RSC Advances

ROYAL SOCIETY
OF CHEMISTRY

www.rsc.org/advances

Journal Name

ARTICLE

Coaxial Yarn Electrode Based on Hierarchical MoS₂ Nanosheets/Carbon Fiber Tows for Flexible Solid-State Supercapacitors

Lili Gao[*a], Xuelian Li[a], Xiaodong Li[b], Jianli Cheng[b], Bin Wang[b], Zhiyu Wang[a], Changming Li[c]

Coaxial yarn electrodes composed of activated carbon fibers tows and MoS₂ nanosheets (ACFTs/MoS₂) are synthesized by a facile hydrothermal approach. The active material, hierarchical MoS₂ nanosheets, delivers high specific capacitance of 308.5 F g^{-1} at scan rate of 5 mV s^{-1}. Solid-state supercapacitors(SCs) in planar format based on the ACFTs/MoS₂ yarn electrode in PVA/H₃PO₄ gel electrolyte show excellent energy density of 3.76 mWh g^{-1} at constant current density of 0.21 A g^{-1}, high power density of 474.49 mW g^{-1} at 3.16 A g^{-1} and long cycle life with a capacitance retention as high as 97.38% even after 6000-time charging-discharging under 2.21A g^{-1}. Furthermore, the SCs in planar format represent superior combination feasibility when combined in parallel or series, approaching to theoretical value. Additionally, twisting SCs made from ACFTs/MoS₂ yarn electrodes show good flexibility and electrochemical stability, which maintain 97.6% of its initial capacitance after being bent to different angles. These outstanding performances can be ascribed to the high accessible surface area for electrolyte, the short path for ion diffusion provided by MoS₂ nanosheets(NSs), as well as the effective transport channels for electron provided by carbon fibers. The rough surface and oxygenous groups on activated carbon fiber offer robust anchor sites for MoS₂ NSs, which not only facilitates the electron transport but also provides strong adhsion between MoS₂ NSs and carbon fibers.

1. Introduction:

All-solid-state supercapacitors (SCs) with high power density, long cycle life, ultralight weight and excellent shape versatility have attracted increasing attention in recent years due to their potential application in digital cameras, all-electric vehicles, and pulse laser techniques. Compared with the conventional flexible SCs with two-dimensional (2D) planar structure,[1-5] one-dimensional (1D) linear SCs shaped in different patterns, such as wire,[6] fiber,[7] yarn,[8] thread,[9] and cable[10] are more promising for portable/wearable electronics, such as smart skins, human friendly devices, flexible/stretchable circuitries and energy devices.[11,12] This flourishing class of electronics can be conformally deformed into complex, non-planar shapes under bending, stretching, compressing or twisting process while maintaining good performance, reliability and integration.

Till now, significant advances have being achieved in the fiber SCs. Carbon nanotubes (CNTs) and graphene are the most widely investigated electrode materials for fibre SCs due to their intrinsic flexibility, light weight and excellent electrical conductivity. The CNT and graphene yarns fabricated by dry or wet spinning methods possess high flexibility, high conductivity and little capacitance reduction even after hundreds of thousands of charge–discharge cycles. However, these yarn electrodes are usually based on the aligned carbon nanotubes or restacking of graphene sheets, which possess low ion-accessible surface area and thus low capacitances (5.38-13.4 F g^{-1} [13, 14] for CNTs and 16.5-46.25 F g^{-1} [15-17] for graphene sheets). To effectively utilize the intrinsic large specific surface area of CNTs and graphene, various new strategies have been developed to increase the ion-accessible surface area of the yarn electrodes by preventing the inter-sheet restacking of graphene sheets[15, 17], using disorderly arrangement of SWNTs,[18] and fabricating the composites of graphene and CNTs[19]. Owing to the enhanced ion-accessible surface area, the resultant graphene and CNT yarns deliver high specific capacitance of 74.6-208.7 F g^{-1};[15, 17-19] however, these strategies may result in poor electron conductivity. For instance, Chen et al.[15] demonstrated that the porous graphene fabricated by the non-liquid-crystal spinning method achieved enhanced ion-accessible surface area and specific capacitance at the expense of electron conductivity of the graphene yarn as compared to that of the graphene yarns by liquid-crystal spinning. The low conductivity of the yarns limits the length of the yarn SCs, which

[a.] College of Environmental Science and Engineering, Taiyuan University of Technology, Taiyuan 030024,Shanxi, Peoples R China

[b.] Institute of Chemical Materials, China Academy of Engineering Physics, Mianyang 621900, Sichuan, Peoples R China

[c] Institute of Clean Energy & Advance Material, Southwest University, Chongqing 400715, Peoples R China

E-mail: gaolili@tyut.edu.cn; Fax: +86 03513176585; Tel: +86 03513176585

is requisite for practical application. For this reason, the yarn SCs with metal wires as current collector and metal oxides as active materials are more promising for practical application. However, the commonly used non-electrochemical activity mental wires, such as Ti wires,[20, 21] Cu wires,[22] Ni wires,[23] and Au wires[24] account for most of the mass or volume of the electrodes, which result in low specific capacitance and energy density. Thus, it is highly desirable to find a current collector with combined advantages of lightweight, highly conductive, electrochemically active and flexible is for the yarn SCs.

Carbon fibres (CFs) are broadly believed to be a promising choice as fibrous substrates due to their good conductivity, lightweight, remarkable mechanical flexibility and low cost.[25] Their high strength and softness are convenient for being woven or knitted into fabrics/textiles for portable/wearable electronics. Moreover, resent report[26] reveals that the commercial CF tows (CFTs) activated by a three-step process have a rough surface with some broken segments, which provide convenience for attachment of the active material.

Of the various active materials, two-dimensional (2D) molybdenum disulfide (MoS_2) has gathered increasing research interests as active material for SCs. As a typical layered transition metal sulfide, MoS_2 is composed of three atomic layers (S-Mo-S) stacked together and bonded through van der Waals interaction. A research hotspot on application of MoS_2 mainly concentrates on fuel cells, solar cells, hydrogen storage and Li-ion batteries.[27-29] Meanwhile, MoS_2 could be anticipated to exhibit good capacitive properties due to their sheet-like morphology, which provides large surface area for double-layer.[30, 31] Charge storage in MoS_2 can potentially occur via three main modes as follows: intersheet, extrasheet double-layer charge storage and faradaic charge transfer process on the centre of transition metal molybdenite that can exhibit a range of oxidation states from +2 to +6.[32] In present state-of-the-art research, MoS_2 based flexible SCs with film format show a high specific capacitance of 243-368 F g^{-1}. In our previous work,[20] a $Ti/TiO_2/MoS_2$ fiber SC with MoS_2 nanosheets (NSs) grown on TiO_2 modified Ti wire shows a mass specific capacitance of 230.2 F g^{-1}(70.6 F cm^{-3}). Owing to the low conductivity and large diameter of the commercial Ti wires, the specific capacitance of the $Ti/TiO_2/MoS_2$ fiber SC is much lower than that of the flexible SCs with film format.

Herein, we report a coaxial yarn electrodes composed of activated CFTs and MoS_2 NSs (ACFTs/MoS_2) by a facial hydrothermal method. The ACFTs show excellent adhesion to MoS_2 due to the defects and oxygenous groups on the surface produced during the activating process. Such an electrode design offers several advantages. Firstly, the 1D CFs serve as the backbone with high flexibility and lightweight, thus permitting the fabrication of collapsible and portable devices. Secondly, the activated CFs with defects and oxygenous groups provide ideal binding sites for MoS_2 NSs attachment. Thirdly, the MoS_2 NSs with the hierarchical structure facilitate fast diffusion of electron/ions from the surface to the inside of the MoS_2 and provide more efficient contact between the ions of the electrolyte and the active materials. All these desirable features contribute to an improved capacity and an enhanced cycle life.

2. Experimental

2.1 Materials

The carbon fiber with an average diameter of 7 μm was purchased commercially from HHKA40, Toho Tenax Co., Japan. Concentrated sulfuric acid (H_2SO_4, 98%), acetone (CH_3COCH_3), ethanol (C_2H_5OH), ammonium persulfate (($NH_4)_2S_2O_8$), sodium hydroxide (NaOH), hexaammonium heptamolybdate tetrahydrate (($NH_4)_6Mo_7O_{24}\cdot4H_2O$), thiourea ($CH_4N_2S$) and phosphoric acid ($H_3PO_4$) were of analytical reagent grade from Chengdu Kelong Chemical Reagent Co., China. Polyvinyl alcohol (PVA, Mw ~13,000) was of analytical reagent grade from Aladdin. All chemical reagents were used directly without any further purification.

2.2 Activation of carbon fiber tows

Prior to the activation of CFTs, a bunch of CFs with total diameter of 70 μm was spun using a motor rotating device as shown in scheme 1I and then self-twisted tightly by adding a kink in the middle of this CFs bunch (scheme 1II), resulting in compact CFTs with about 140 μm in diameter (scheme 1III), so that the conductivity and assembling feasibility were improved.

Activation of the obtained CFTs involves two steps: annealing in air, oxidation by $H_2SO_4/(NH_4)_2S_2O_8$. In the first step, the pristine CFTs were initially annealed in air at 400 ^{0}C for 20 min to remove the rubber, and then cleaned through sonication for 10 min in deionized water, acetone, and ethanol successively to get rid of oil, followed by drying in air at room temperature. In the second step, the cleaned and dried CFTs were oxidized by immersing into a 40 ml mixture solution containing 100mL/L H_2SO_4 and 200g/L ($NH_4)_2S_2O_8$ at 30-40ºC under stirring until no bubbles appeared, and then washed with NaOH (10%, w/w), deionized water until the pH of solution became neutral, followed by drying in heat oven. The activated CFTs were obtained as seen in scheme 1IV for further growth of MoS_2 NSs.

2.3 Synthesis of ACFTs/MoS_2 Yarn Electrode

The activated CFTs (ACFTs) were put into a 50 mL Teflon-lined stainless steel autoclave for hydrothermal growth of MoS_2 NSs to produce ACFTs/MoS_2 yarns as shown in scheme 1V. The specific steps for MoS_2's hydrothermal systhsis were similar with previous reports.[20,33] More experimental details are shown in Supporting Information. The loaded mass of MoS_2on ACFTs was measured by weighing method. In comparison, the self-twisting pristine CFs (without activation) were undergoing the same hydrothermal process mentioned above to obtain CFTs/MoS_2 yarns.

2.4 Assembling of ACFTs/MoS_2 SCs

For all SCs, PVA-H_3PO_4 gel was used as electrolyte. The PVA-H_3PO_4 gel was prepared as following: PVA (1 g) was dissolved in deionized water (10 g) at 95 ºC under vigorous stirring until the polymer dissolved completely in water to form clear solution, followed by adding of H_3PO_4 (1 g) and stirring for 60 min at room temperature to get transparent, viscous gel.

(1) Assembling of ACFTs/MoS₂ SC in planar format

Two ACFTs/MoS₂ yarn electrodes were placed symmetrically on PET substrate with *approx*. 1 mm distance and one end of which attached to conducting cloth, followed by a thin layer of PVA-H₃PO₄ gel electrolyte on them to make a planar pattern SC as seen in Figure 3a.

(2) Assembling of ACFTs/MoS₂ combined devices

Multiple ACFTs/MoS₂ planar pattern SCs were combined in parallel or series as shown in Figures 5a and 5b.

(3) Assembling of ACFTs/MoS₂ twisting SC

Two ACFTs/MoS₂ yarns were coated with PVA-H₃PO₄ gel and dried at room temperature for 6h. Then, they were twisted together and coated with PVA-H₃PO₄ gel again to make a twisting SC (Figure 6a). No separator was used in the solid device.

2.5 Characterization and Instrumentation

(1) Yarn characterization

The morphology of ACFTs/MoS₂ coaxial yarn electrodes was characterized using field emission scanning electron microscopy (FE-SEM, Hitachi S-4800). The structure of the MoS₂ NSs was investigated by transmission electron microscopy (TEM, FEI Tecnai F20) with energy dispersive X-ray analysis system (EDS). Raman scattering spectrum (conducted on Jobin-Yvon LabRam HR80 spectrometer equipped with a 532nm line of Torus 50 mW diode-pumped solid-state laser) was carried out to analyze the structures of electrode. The specific surface areas of pristine and activated CFTs were calculated by the Brunauer-Emmett-Teller (BET) analysis of the nitrogen adsorption measurements (JW-BK300, JWGB SCI&TECH Co., China). A FTIR spectrometer (Thermo Nicolet Co., USA) was employed to examine the infrared spectra of samples using a pressed KBr tablet method. The surface of ACFTs/MoS₂ yarn was further investigated using X-ray photoelectron spectroscopy (XPS, ESCALAB-210) with Al Kα radiation (1486.6 eV).

(2) Electrochemical testing

To evaluate the electrochemical performance, cyclic voltammetry (CV) and electrochemical impedance spectroscopy (EIS) were performed on Electrochemical Workstation (VMP3, Bio-Logic, France) and galvanostatic charge-discharge (GCD) measurements were conducted on Arbin BT2000 Battery Test Station. EIS was measured at open-circuit voltage in a frequency range from 100 mHz to 100 kHz with a potential amplitude of 10 mV. All measurements were carried out at room temperature. Detailed information about the calculations of mass specific capacitance (C_m), volumetric specific capacitance (C_v), mass energy density (E_m), volumetric energy density (E_v), mass power density (P_m) and volumetric power density (P_v) were given in the Supporting Information.

3. Results and Discussion

3.1. Characterization of ACFTs/MoS₂ Yarn

The structure and morphology of ACFTs/MoS₂ characterized by SEM are shown in Figure 1. SEM images in Figures 1a and 1b show that ACFTs/MoS₂ yarn electrode consists of bundles of CFs and the whole surface of the activated CF is homogeneously covered by typical hierarchical MoS₂ NSs active layer. The thickness of MoS₂ NSs is estimated to be about 10 nm as marked by arrows in Figure 1b. As illustrated in cross-sectional SEM images of Figures 1c and 1d, MoS₂ active layer is successfully grown on CF in the form of surface cladding, forming a typical coaxial cable-like structure, where the inner carbon fiber is about 7μm in diameter and the uniform coating of MoS₂ active layer has a thickness of *approx*. 150 nm. Additionally, the formation of MoS₂ active materials was confirmed by XPS spectrum in Figures S3c, in which two characteristic peaks at 229.1 and 232.2eV corresponding to the Mo 3d5/2 and Mo 3d3/2 orbitals suggest a Mo (IV) characteristic in MoS₂, and the binding energies located at 162.0 and 163.3eV are due to S 2p3/2 and 2p1/2 of MoS₂.[34]

The nanostructure of MoS₂ was further investigated using TEM and HRTEM. ACFTs/MoS₂ yarn was firstly cut into pieces, and then dispersed in aqueous solution by ultrasonic. Subsequently the solution was cast on a copper wire mesh and rapidly evaporated in hot oven for TEM and HRTEM. In agreement with the above-described SEM observations, the inner CF can be hardly observed in Figure 2a because of uniform coating layer of MoS₂ NSs with 10 nm in thickness. More importantly, it is worth noting that, during the preparation process of TEM sample, even after a vigorous sonication, the MoS₂ NSs are still firmly attached to the surface of CF,
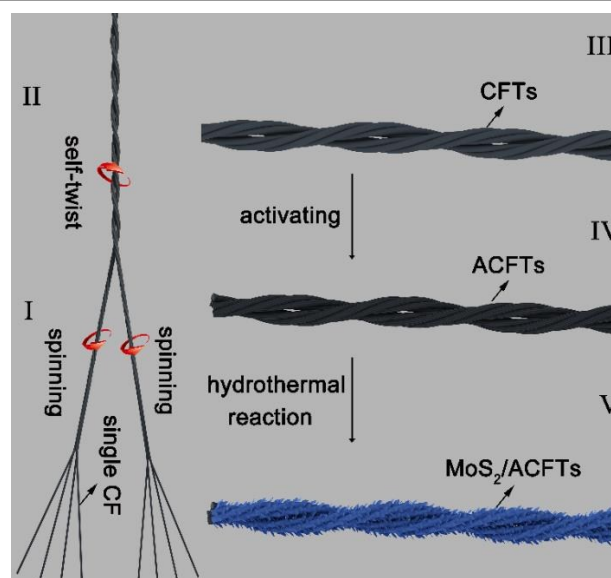
Scheme 1. Illustration of preparation process for ACFTs/MoS₂ yarn electrode.
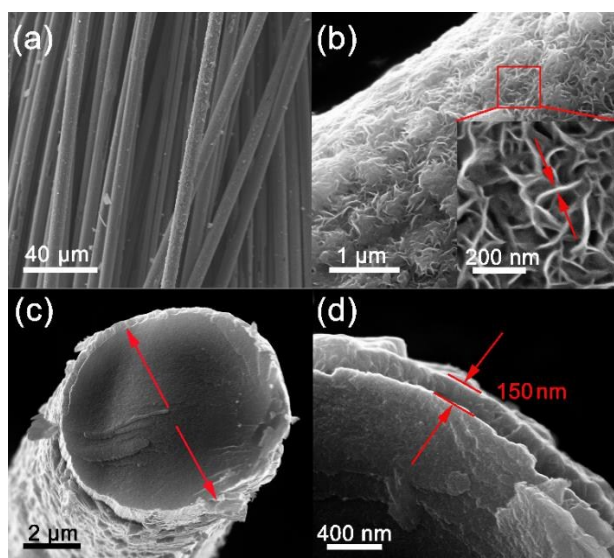
Figure 1. SEM images of ACFTs/MoS. Low-magnification SEM image of ACFTs/MoS$_2$ (a); High-magnification SEM image of MoS$_2$ NSs wrapped on ACFT (b); the cross-sectional SEM image of the ACFT/MoS$_2$ coaxial structure (c-d).

suggesting the strong and effective interfacial bonding between MoS$_2$ active layer and CF.[34] HRTEM images in Figures 2b and 2c reveal that MoS$_2$ NSs are composed of a few layers with interplanar spacing of 0.65 nm associated with the (002) plane of MoS$_2$.[35] Typical lamellar structure of MoS$_2$ was further confirmed by Raman spectra in Figures 2d and 2e, in which, two distinct peaks around at the bands of 374 and 404 cm^{-1} are MoS$_2$ characteristic signature, corresponding to in-plane E$^1_{2g}$ (in-

plane displacement of Mo and S atoms) and to out-of-plane A^1_g (out-of-plane symmetric displacements of S atoms along the c-axis) Raman mode,[34] respectively. Furthermore, two obvious peaks at 1367 and 1592 cm^{-1} characteristic of D and G bands of carbon materials [13, 14] could be seen for both CFTs and ACFTs in Figure 2d, but totally disappear for ACFTs/MOS$_2$, indicating that the coating MoS$_2$ active layer on the surface of CF (~150 nm in thickness) is very impact and uniform, so that the characteristic peaks for CF can hardly be detected by Raman spectra. The chemical composition of ACFTs/MoS$_2$ are determined by EDS spectra in Figure 2f, which exhibit the presence of C, Mo, S (Cu due to the Cu grid, O due to the activation process). From the aforementioned results and illustration, it is safely concluded that MoS$_2$ NSs are successfully grown on carbon fiber to form coaxial structure and furthermore the adhesion between them is strong.

To further investigate the effect of CFTs' activation process on the growth of MoS$_2$ NSs on ACFTs' surface, the morphology, specific surface area, pore size and functional groups were measured by SEM, nitrogen gas adsorption/desorption technique, FTIR and XPS spectra as shown in Figure2 S1 and S2. From the SEM images in Figures S1a and S1b, the surface of activated carbon fiber (ACF) is coarser with carved grooves than CF. The specific surface area of ACFTs is 11.4 m^2 g^{-1} calculated from the nitrogen gas adsorption/desorption curves in Figure S2a, which is about 5.4-fold higher than that of the CFTs (2.1 m^2 g^{-1}). Furthermore, ACFTs' nitrogen gas adsorption/desorption curve shows a hysteresis loop at high relative pressure characteristic of type IV isotherm, indicating the existence of plentiful mesopores in ACFTs.[36]
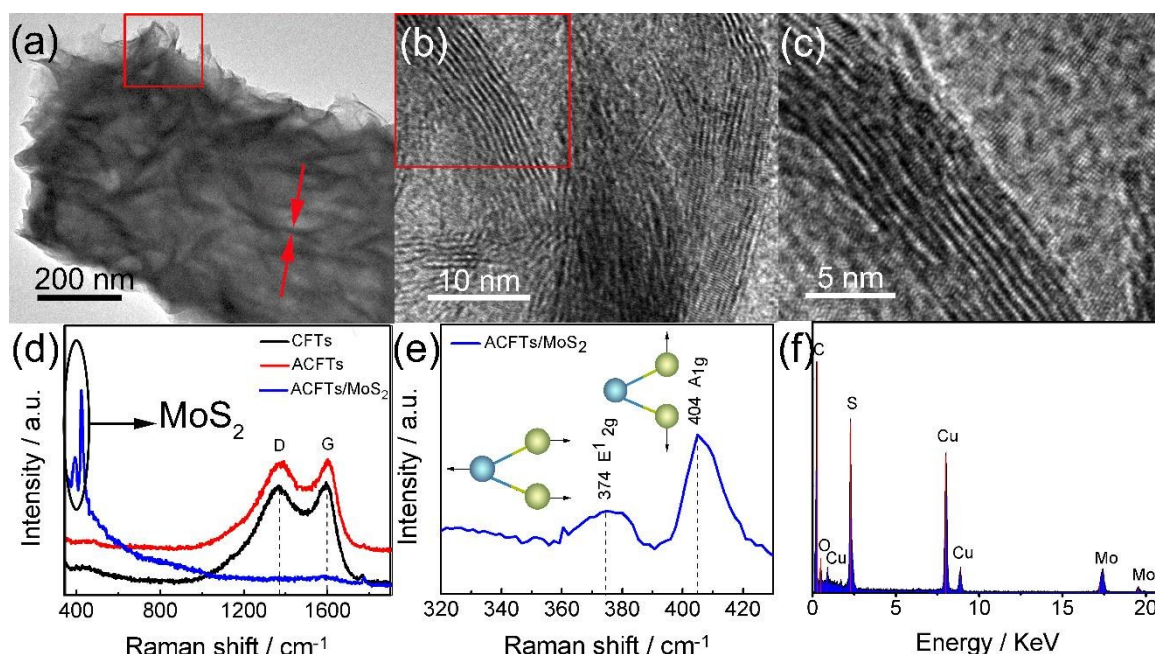
Figure 2. Properties of the ACFTs/MoS$_2$. TEM image of ACFTs/MoS$_2$ slice being exfoliated from ACFTs/MoS$_2$ yarn by ultrasonic (a); HRTEM images of MoS$_2$ NSs (b-c); Raman spectra (d) of the pristine CFTs, ACFTs and ACFTs/MoS$_2$; Magnified Raman spectrum (e) of ACFTs/MoS$_2$ as marked in 2d; EDS spectra of ACFTs/MoS$_2$ (f).
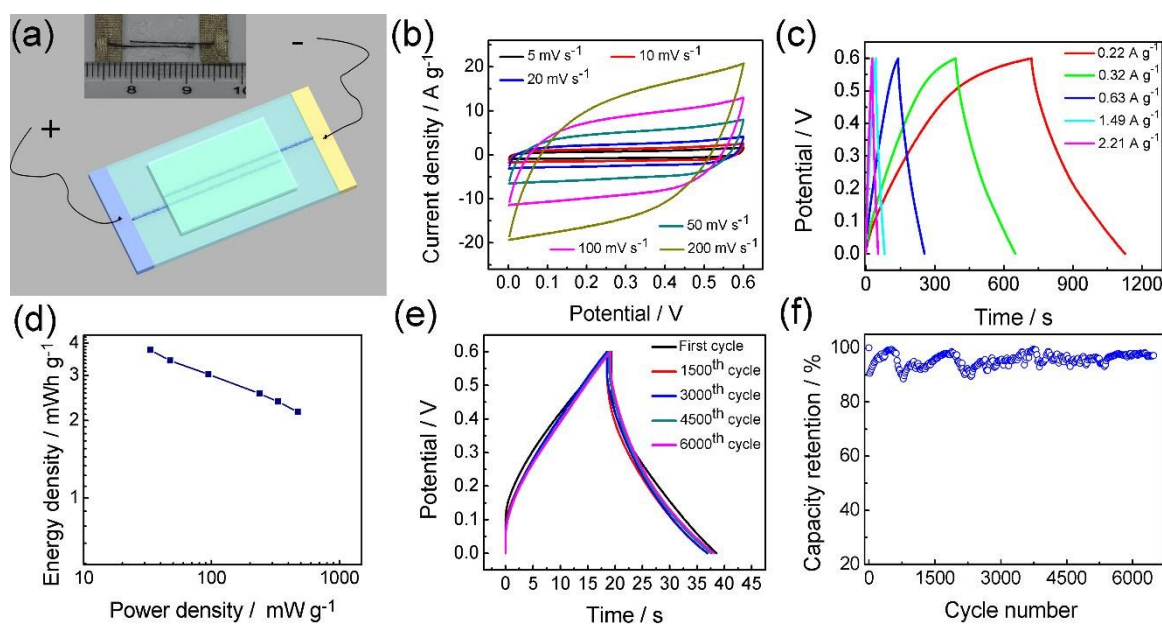
Figure 3. Electrochemical performance of ACFTs/MoS$_2$ yarn electrode in symmetrical planar pattern SC. Schematic illustration and digital photograph (Inset) of ACFTs/MoS$_2$ planar pattern SC (a); CV performances at different scan rates under voltage window between 0V to +0.6V (b); GCD performances under different current densities (c); The Ragone plots (d); Cycling performance at current density of 2.21 A g^{-1} (e); Plot of capacity retention *vs*. cycle number (f).

This could also be verified by pore size results in Figure S2b. The pore sizes for ACFTs, calculated from desorption data using Barrette-Joynere-Halenda (BJH) model, mainly distribute in the range from 2.2 nm to 20 nm, indicating the mesoporous structure of the ACFTs. Through activation steps, the average pore size of CFTs decreases from original 41.2 nm to 10.3nm. This is the explanation for higher surface area.[13] The functional groups on surface of ACFTs were further examined by FTIR spectra and XPS as shown in Figure S3. In the FTIR spectra(Figure S3a), a peak at 1407 cm^{-1} characteristic of carbonyl group (C-O) can be only found in ACFTs sample, combined with the vibrational mode (stretching) of O-H and C=O groups located at 3449 and 1632 cm^{-1}, respectively, confirming the successful introducing of carboxyl and hydroxyl groups. This can be also verified by corresponding C-O, O-C=O bonds of XPS spectrum of C1s seen in Figure S3e and C=O, O-H bonds of XPS spectrum of O1s seen in Figure S3f. It can be also predicted that the wettability of activated CFTs is improved. In conclusion, the activation process plays an important role in increasing CFTs' specific surface area, decreasing the pore size and introducing hydrophilic oxygenous groups such O-H and C=O, which may supply more sites and stronger interaction for subsequent MoS$_2$ NSs growth. This point was as well certified by the XPS spectra in Figure S3c and S3f, in which, the Mo-O bonds could be obviously seen in Mo3d (at 236.1 eV) and O1s (at 531.0 eV). Excluding the existence of any molybdenum oxide (MoOx) from Roman and XPS analysis[37,38], it could be boldly inferred that the Mo-O bonds are derived form the interaction between MoS$_2$ and the oxygenous groups on ACFs.

3.2. Electrochemical performances of ACFTs/MoS$_2$

3.2.1 Electrochemical performances of ACFTs/MoS$_2$ planar pattern SC

Planar pattern SC is the most common and simplest SC, furthermore, being considered as a conventional method to investigate the electrochemical performances of electrode. The symmetric planar solid-state SC based on ACFTs/MoS$_2$ yarn electrode was fabricated as shown in Figure 3a. To obtain good electrochemical performance, the hydrothermal reaction time was firstly optimized. CV curves with different hydrothermal time were compared in Figures S4a and S4b, revealing that ACFTs/MoS$_2$ exhibit the optimized capacitive behaviour when the hydrothermal time is 9h, therefore, all the below-mentioned ACFTs/MoS$_2$ coaxial yarn were prepared in this condition. From the CV curves of ACFTs/MoS$_2$ under different electrochemical voltage windows at scan rate of 10 mV s^{-1} in Figure S5a, it could be inferred that 0.6 V is the upper limit of voltage window for ACFTs/MoS$_2$ symmetric solid-state SC to maintain stable electrochemical performance. GCD performances in Figure S5b under different voltage windows at 0.63 A g^{-1} prove this inference. Under the voltage window of 0.6 V, the shapes of CV curves for ACFTs/MoS$_2$ are slightly changed with the increase of scan rates, and can still retain its double-layer capacitive behaviour at a fast scan rate of 200 mV s^{-1} as shown in Figure 3b. GCD measurements (Figure 3c) collected at different current densities further indicate an ideal capacitive behaviour and fast charge/discharge properties of ACFTs/MoS$_2$ yarn electrodes. Notably, a substantially small IR drop (0.0028V) at the charging/discharging current density of 0.22 A g^{-1} can be got, implying a low internal resistance. The Ragone plots in Figure 3d show the energy and power densities of ACFTs/MoS$_2$ SC. The maximum energy density of 3.76 mWh g^{-1} (4.04 mWh cm^{-3}) at a power density of 33.21 mW g^{-1} (specific current of 0.21 A g^{-1}) and the maximum power density of 474.49 mW g^{-1}
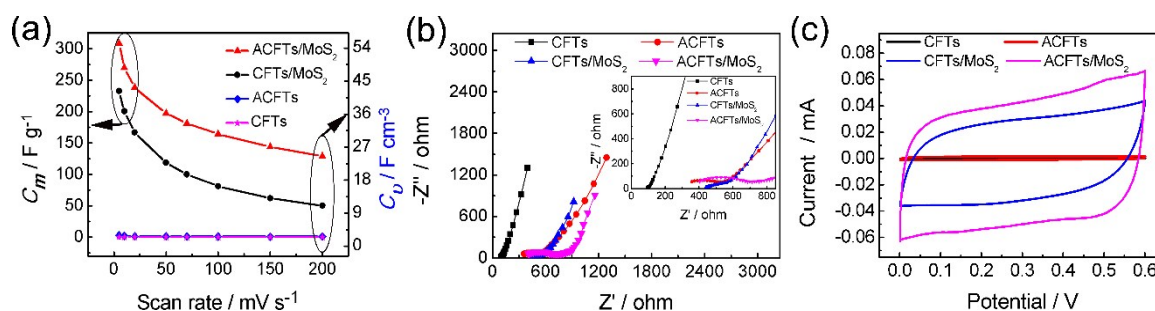
Figure 4. Comparison of electrochemical performance among ACFTs/MoS$_2$, CFTs/MoS$_2$, ACFTs and CFTs yarn electrodes. Plots of specific capacitance vs scan rate (a); Nyquist plots (b); CV curves at 10 mV s^{-1} (c).
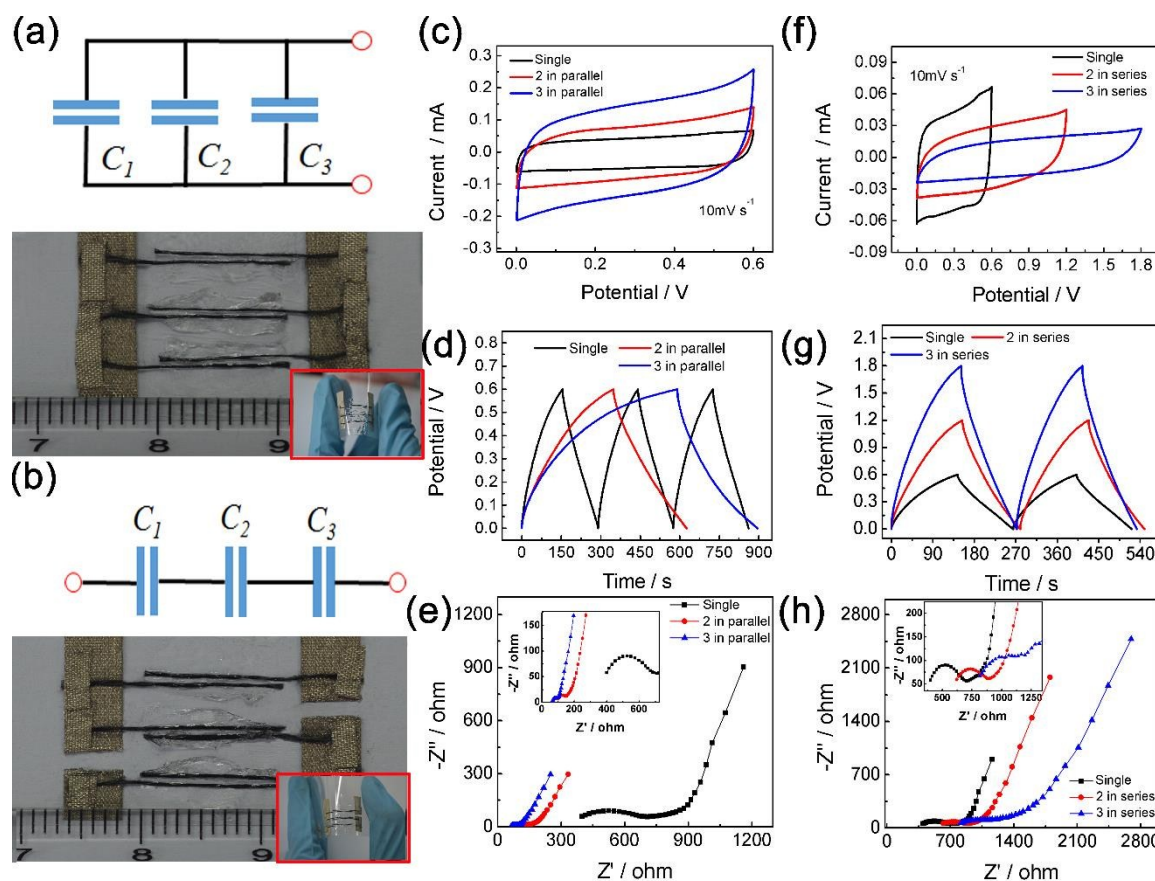
Figure 5. Schematic illustration and digital photograph of ACFTs/MoS$_2$ planar pattern SCs in parallel and series combination circuits (a-b); CV (c), GCD (d) and Nyquist (e) performances of devices combined using single, double or triple planar pattern SCs in parallel; CV (f), GCD (g) and Nyquist (h) performances of devices combined using single, double or triple planar pattern SCs in series.

(509.55 mW cm^{-3}) at an energy density of 2.16 mWh g^{-1} (specific current of 3.16 A g^{-1}) can be achieved at an operating voltage of 0.6 V. Figure 3e displays the charging-discharing performance of these ACFTs/MoS$_2$ yarn electrodes at a large current density of 2.21 A g^{-1}. ACFTs/MoS$_2$ yarn electrodes show high electrochemical stability, which can retain about 97.38% of their initial specific capacitance after 6000 cycles as shown in Figure 3f, demonstrating the excellent long-term cycling stability. The excellent electrochemical stability indicates that the MoS$_2$ active layer could be mechanically stable during the cycling tests. It is worthy noting, the charging-discharing measurements were conducted under room temperature, so

that the ups and downs of the capacitance retention curve of ACFTs/MoS$_2$ yarn electrodes occurred at the previous cycles might be caused by the temperature difference between day and night. (Day temperature was recorded about 15 ^{o}C and night temperature was about 5 ^{o}C.). To verity the inference, the SC was specifically measured under controlled temperature, shown as in Figure S5c and Supporting Information, indicating that SC show more excellent capacitance under higher temperature, which might be because high temperature accelerates the transfer of ions in the gel electrolyte thus improving the capacitance of these electrodes.[39, 40] Another possible explanation might be the excess of MoS$_2$ NSs that are not fully utilized. With the ongoing cycling, because of the

gradually penetration of electrolyte and improved stability of structure of MoS$_2$ NSs, the capacity of the ACFTs/MoS$_2$ electrode maintains stable.

To further understand the effect of activating process on electrochemical performance, different yarn electrodes (ACFTs/MoS$_2$, CFTs/MoS$_2$, ACFTs and CFTs) were assembled into symmetric planar pattern SCs and their electrochemical performance were measured as shown in Figure 4. From the plots of specific capacitance *vs* scan rate for different yarn electrodes (Figure 4a), the specific capacitance for ACFTs/MoS$_2$ is highest (308.45 F g^{-1} or 55.21 F cm^{-3}) at 5 mV s^{-1}, followed by CFTs/MoS$_2$ (232.87 F g^{-1}, 37.23 F cm^{-3}), increasing by 33%. The better rate capability and higher specific capacity for ACFTs/MoS$_2$ coaxial yarn electrode might be attributed to two reasons: the stronger adhesion between MoS$_2$ NSs and the surface of activated CF, leading to faster electron transfer and lower electron resistence; the larger specific surface areas, resulting in higher load of MoS$_2$. The equivalent series resistance, charge transport and ion diffusion of different SCs were measured by EIS, as shown in Figure 4b. The x-intercept of the Nyquist plots represents the equivalent series resistance (*ESR*) of two-electrode SC and the charge transport resistance (*Rct*). The slope of the Nyquist plots, known as the Warburg resistance (*Z*w), is a result of the frequency dependence of ion diffusion in the electrolyte to the electrode interface.[41, 42] From qualitative perspective, *ESR* of ACFTs is much larger than that of CFTs which is reasonable because of the introduction of oxygenous groups. On the contrary, the *ESR* of ACFTs/MoS$_2$ is lower than the corresponding values of CFTs/MoS$_2$, being exactly consistent with the trend of the capacitance plots and indirectly confirming the strong adhesion between MoS$_2$ NSs and ACFTs. The CV curves of different SCs at scan rate of 10 mV s^{-1} are shown in Figure 4c, in which it can be seen the SC based on ACFTs/MoS$_2$ electrode shows best performance, followed by CFTs/MoS$_2$, ACFTs, and last CFTs. It should be specially pointed out that ACFTs and CFTs exhibit much smaller capacitance compared to ACFTs/MoS$_2$ and CFTs/MoS$_2$ being coated with MoS$_2$ active layer, proving that CFTs and ACFTs mainly act as medium for electron transfer and make negligible contribution to capacitance, while MoS$_2$ play critical role in SC's capacity. To further understand the capacitance of hierarchical MoS$_2$ active layer synthesized on ACFTs in our work, it is compared with other work reported recently, as shown in Figure S5d, indicating a better or at least comparable performance.

3.2.2 Electrochemical performances of ACFTs/MoS$_2$ SCs combined devices

As illustration above, for a single SC device, its operating voltage can achieve 0.6 V and its high specific capacitance can reach to 308.5 F g^{-1}. However, the potential and capacitance might be too limited to meet the requirements for some practical micro-electronics application. Thus, multiple SCs may have to be connected together in series and/or in parallel in order to produce reasonable output potential and rational specific capacitance.

Figures 5a and 5b are circuit diagrams and digital photographs of three real SCs connected in parallel and series,

respectively. Figures 5c and 5d show CV and GCD curves of three SCs connected in parallel. As compared with a single SC, the output current of the assembled parallel devices is increased by a factor of three under the same voltage window of 0 to 0.6V. Correspondingly, the discharge time is about three times longer than that of a single device, which means approximately triple capacitance could be achieved. For three SCs combined in series of Figures 5f and 5g, under the similar discharge time, the output voltage of this device can be extended to 1.8 V, whereas a single one can only operate below 0.6 V. However, the series devices of three SCs made sacrifice that their capacitance decreased only one-third. In general, similar to a single one, the integrated devices (in series or parallel) exhibit rectangular-like CV curves and reasonably symmetrical and linear GCD curves, which again indicate the excellent capacitive properties of ACFTs/MoS$_2$ SCs. As Nyquist plots of devices connected in series or parallel shown in Figures 5e and 5h, the shapes of EIS curves for the combinations are similar to that of a single SC. It is easily found that ESR of a sample device is 398.9 Ω. For the case of three series devices, ESR is 816.5 Ω, about triple ESR of a single one. ESR of the three parallel devices is about 64.8 Ω, which is slightly lower than the total theoretical ESR of parallel SCs. These results are close to the expected ones for the two different combinations.

Overall, these results illustrate that electrical performances of the series and parallel combinations of the SC devices, which show a good agreement with the theoretical models of series and parallel combined circuits, enabling them to combine multiply for practical applications.

3.2.3 Electrochemical performances of ACFTs/MoS$_2$ twisting yarn SC

For the realization of fiber-based wearable electronics, the most important consideration is the development of sustainable flexible systems which support high carrier mobility and good overall electrical performance, combined with mechanical and environmental stability.
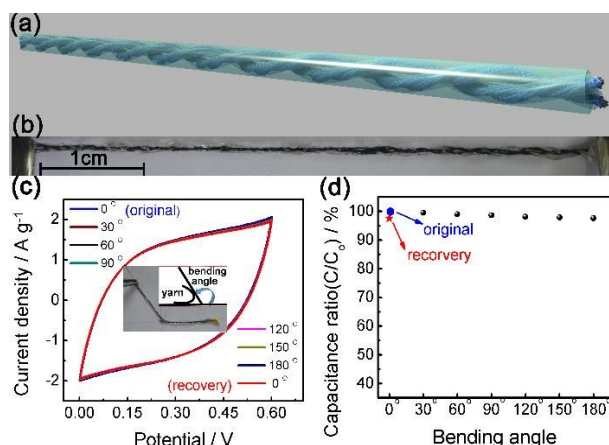
Figure 6. Schematic illustration (a) and digital photograph (b) for preparation of ACFTs/MoS$_2$ twisting yarn SC; (c) CV performance of ACFTs/MoS$_2$ twisting yarn SC under different bending angles at scan rate of 10 mV s-1, the insets are the digital photo of yarn SC bent to 60o and schematic diagram of bending. (d) Capacitance ratio (C/Co, where Co is the initial capacitance) versus bending angles for yarn SCs.

Based on great capacitive behaviour and high flexibility of ACFTs/MoS$_2$ yarn electrode, a yarn SC was fabricated by further intertwining two ACFTs/MoS$_2$ yarn electrodes with H$_3$PO$_4$-PVA gel polyelectrolyte (Figure 6a).The solid-state electrolyte for the yarn SC will overcome the major drawbacks of conventional liquid electrolytes, such as leakage of electrolyte, difficulty in device integration and environmental stability, which are crucial for the development of useful wearable fiber devices. Apart from acting as the electrolyte, the coating layer of H$_3$PO$_4$-PVA gel along the whole ACFTs/MoS$_2$ could also function as an effective separator to prevent the undesirable short circuit of two electrodes. Note that before intertwining two ACFTs/MoS$_2$ yarns, each yarn should be entirely wrapped by a layer of H$_3$PO$_4$-PVA gel electrolyte, which also can prevent the original twisted structure of ACFTs from untwisting, in other words, can retain the twisting structure in order to further assemble the yarn-shaped SC. The resulting SC maintains a good yarn shape with length of 5.5 cm and the intertwining structure of two ACFTs/MoS$_2$ electrodes covered with H$_3$PO$_4$-PVA gel electrolyte is shown in Figure 6b. A ACFTs/MoS$_2$ twisting yarn SC was bent to 30°, 60°, 90°, 120°, and 150° and 180°, and the capacitance performances with bending angles were shown in Figures 6c and 6d. No obvious damages could be found in structure, meanwhile, almost overlapped CV curves are observed for the ACFTs/MoS$_2$ yarn SC deformed with different bending angles. Furthermore, when yarn SC was recovered to original state, the recovery capacitance can maintain 97.6% of its original capacitance as shown in Figure 6d. In conclusion, the ACFTs/MoS$_2$ yarn electrode represents high flexibility and electrochemical stability, which is promising to power various miniaturized and wearable electronic devices.

Conclusions

In summary, ACFTs/MoS$_2$ coaxial yarn electrodes have been easily fabricated by a simple hydrothermal method, prior to which activating treatment plays a crucial role in assisting MoS$_2$ NSs being more uniformly and tightly anchored on the surface of CF, leading to faster electron transfer and lower electron resistance. ACFTs/MoS$_2$ coaxial yarn electrodes deliver remarkable electrochemical performance with a high capacitance (308.45 F g^{-1}, 55.21 F cm^{-3} at 5 mV s^{-1}). The SCs based on the electrode represent good rate capability and superior cycling stability at a high current density of 2.21 A g^{-1} (about 97.38% specific capacitance retained after 6000 cycles). The maximum energy density of 3.76 mWh g^{-1} (4.04 mWh cm^{-3}) at a power density of 33.21 mW g^{-1} (specific current of 0.21 A g^{-1}) and the maximum power density of 474.49 mW g^{-1} (509.55 mW cm^{-3}) at an energy density of 2.16 mWh g^{-1} (specific current of 3.16 A g^{-1}) can be achieved at an operating voltage of 0.6 V.

ACFTs/MoS$_2$ coaxial yarn electrodes have been further assembled into SC devices by being connected in parallel or series, showing excellent electrical performances. The ACFTs/MoS$_2$ electrodes were additionally twisted to product yarn SCs, representing stable electrochemical performances with being bent. All these show a great potential in various

fields, e.g., being easily integrated into electronic textiles by conventional weaving technique.

Acknowledgements

Notes and references

1　M. S. Javed, S. Dai, M. Wang, D. Guo, L. Chen, X. Wang, C. Hu and Y. Xi, *J. Power Sources*, 2015, **285**, 63-69.
2　K. Krishnamoorthy, G. K. Veerasubramani, P. Pazhamalai and S. J. Kim, *Electrochim. Acta*, 2016, **190**, 305-312.
3　G. Sun, J. An, C. K. Chua, H. Pang, J. Zhang and P. Chen, *Electrochem. Commun.*, 2015, **51**, 33-36.
4　B. Yao, L. Yuan, X. Xiao, J. Zhang, Y. Qi, J. Zhou, J. Zhou, B. Hu and W. Chen, *Nano Energy*, 2013, **2**, 1071-1078.
5　B. G. Choi, S.-J. Chang, H.-W. Kang, C. P. Park, H. J. Kim, W. H. Hong, S. Lee and Y. S. Huh, *Nanoscale*, 2012, **4**, 4983-4988.
6　P. Xu, B. Wei, Z. Cao, J. Zheng, K. Gong, F. Li, J. Yu, Q. Li, W. Lu and J.-H. Byun, *ACS nano*, 2015, **9**, 6088-6096.
7　X. Xiao, T. Li, P. Yang, Y. Gao, H. Jin, W. Ni, W. Zhan, X. Zhang, Y. Cao, J. Zhong, L. Gong, W.-C. Yen, W. Mai, J. Chen, K. Huo, Y.-L. Chueh, Z. L. Wang and J. Zhou, *ACS Nano*, 2012, **6**, 9200-9206.
8　Y. Shang, C. Wang, X. He, J. Li, Q. Peng, E. Shi, R. Wang, S. Du, A. Cao and Y. Li, *Nano Energy*, 2015, **12**, 401-409.
9　Q. Meng, K. Wang, W. Guo, J. Fang, Z. Wei and X. She, *Small*, 2014, **10**, 3187-3193.
10　S. T. Senthilkumar and R. Kalai Selvan, *Phys. Chem. Chem. Phys.*, 2014, **16**, 15692-15698.
11　K. Jost, D. Stenger, C. R. Perez, J. K. McDonough, K. Lian, Y. Gogotsi and G. Dion, *Energy Environ. Sci.*, 2013, **6**, 2698-2705.
12　D. Yu, Q. Qian, L. Wei, W. Jiang, K. Goh, J. Wei, J. Zhang and Y. Chen, *Chem. Soc. Rev.*, 2015, **44**, 647-662.
13　F. Su, X. Lv and M. Miao, *Small*, 2015, **11**, 854-861.
14　H. Sun, X. You, J. Deng, X. Chen, Z. Yang, J. Ren and H. Peng, *Adv. Mater.*, 2014, **26**, 2868-2873.
15　S. Chen, W. Ma, Y. Cheng, Z. Weng, B. Sun, L. Wang, W. Chen, F. Li, M. Zhu and H.-M. Cheng, *Nano Energy*, 2015, **15**, 642-653.
16　Y. Meng, Y. Zhao, C. Hu, H. Cheng, Y. Hu, Z. Zhang, G. Shi and L. Qu, *Adv. Mater.*, 2013, **25**, 2326-2331.
17　G. Huang, C. Hou, Y. Shao, B. Zhu, B. Jia, H. Wang, Q. Zhang and Y. Li, *Nano Energy*, 2015, **12**, 26-32.
18　Q. Meng, H. Wu, Y. Meng, K. Xie, Z. Wei and Z. Guo, *Adv. Mater.*, 2014, **26**, 4100-4106.
19　H. Cheng, Z. Dong, C. Hu, Y. Zhao, Y. Hu, L. Qu, N. Chen and L. Dai, *Nanoscale*, 2013, **5**, 3428-3434.
20　X. Li, X. Li, J. Cheng, D. Yuan, W. Ni, Q. Guan, L. Gao and B. Wang, *Nano Energy*, 2016, **2**, 1228-237.
21　T. Chen, L. Qiu, Z. Yang, Z. Cai, J. Ren, H. Li, H. Lin, X. Sun and H. Peng, *Angew. Chem. Int. Ed.*, 2012, **51**, 11977-11980.

RSC Advances Accepted Manuscript

22 Z. Yu and J. Thomas, *Adv. Mater.*, 2014, **26**, 4279-4285.
23 Q. Wang, X. Wang, J. Xu, X. Ouyang, X. Hou, D. Chen, R. Wang and G. Shen, *Nano Energy*, 2014, **8**, 44-51.
24 H. Xu, X. Hu, Y. Sun, H. Yang, X. Liu and Y. Huang, *Nano Research*, 2015, **8**, 1148-1158.
25 N. Yu, H. Yin, W. Zhang, Y. Liu, Z. Tang and M.-Q. Zhu, *Adv. Energy Mater.*, 2015, **6**, 1614-6840.
26 D. Yu, S. Zhai, W. Jiang, K. Goh, L. Wei, X. Chen, R. Jiang and Y. Chen, *Adv. Mater.*, 2015, **27**, 4895-4901.
27 S. K. Pradhan, B. Xiao and A. K. Pradhan, *Sol. Energy Mater. Sol. Cells*, 2016, **144**, 117-127.
28 X. Zhang, Q. Zhang, Y. Sun, P. Zhang, X. Gao, W. Zhang and J. Guo, *Electrochim. Acta*, 2016, **189**, 224-230.
29 M. Wang, G. Li, H. Xu, Y. Qian and J. Yang, *ACS Appl. Mat. Interfaces*, 2013, **5**, 1003-1008.
30 M. Yang, J.-M. Jeong, Y. S. Huh and B. G. Choi, *Compos. Sci. Technol.*, 2015, **121**, 123-128.
31 M. Acerce, D. Voiry and M. Chhowalla, *Nat Nano*, 2015, **10**, 313-318.
32 M. S. Jia and K. P. Loh, *Electrochem. Solid-State Lett.*, 2007, **10**.
33 J. Xie, H. Zhang, S. Li, R. Wang, X. Sun, M. Zhou, J. Zhou, X. W. D. Lou and Y. Xie, *Adv. Mater.*, 2013, **25**, 5807-5813.
34 J. Zhou, J. Qin, X. Zhang, C. Shi, E. Liu, J. Li, N. Zhao and C. He, *ACS Nano*, 2015, **9**, 3837-3848.
35 Y. Lu, X. Yao, J. Yin, G. Peng, P. Cui and X. Xu, *RSC Adv.*, 2015, **5**, 7938-7943.
36 W. Ma, S. Chen, S. Yang, W. Chen, Y. Cheng, Y. Guo, S. Peng, S. Ramakrishna and M. Zhu, *J. Power Sources*, 2016, **306**, 481-488.
37 W. J. Dong, J. Ham, G. H. Jung, J. H. Son and J. L. Lee, *J. Mater. Chem. A*, 2016, **4**, 4755-4762.
38 B. C. Windom, W. G. Sawyer and D. W. Hahn, *Tribol. Lett.*, 2011, **42**, 301-310.
39 G. Xiong, A. Kundu and T. S. Fisher, in *Thermal Effects in Supercapacitors*, *First Edition*, Springer, 2015.
40 M. Bielejewski, A. Puszkarska and J. Tritt-Goc, *Electrochim. Acta*, 2015, **165**, 122-129.
41 K. Wang, Q. Meng, Y. Zhang, Z. Wei and M. Miao, *Adv. Mater.*, 2013, **25**, 1494-1498.
42 Y. Zhu, Z. Wu, M. Jing, H. Hou, Y. Yang, Y. Zhang, X. Yang, W. Song, X. Jia and X. Ji, *J. Mater. Chem. A*, 2014, **3**, 866-877.

Graphical and Textual Abstract
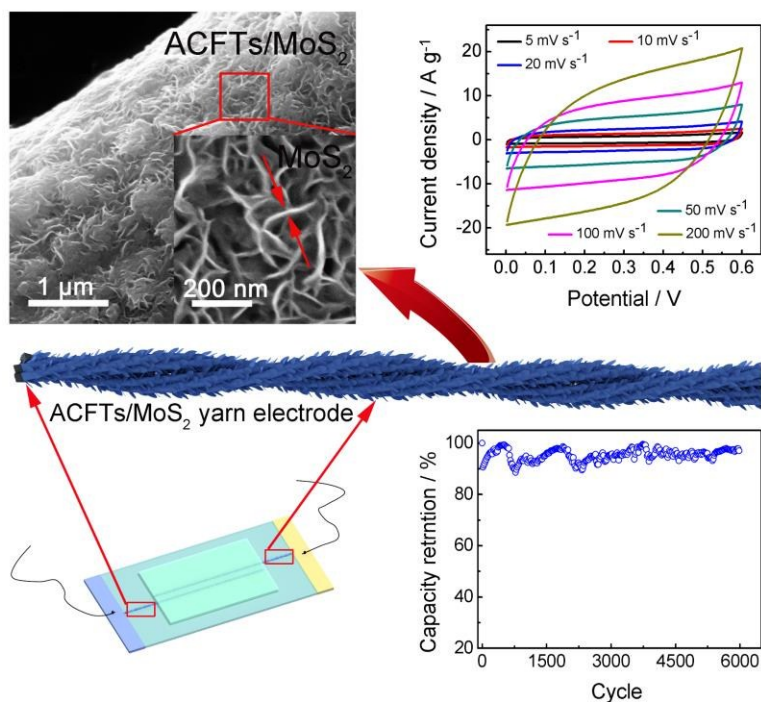
The carbon fiber tows/hierarchical MoS$_2$ nanosheets (ACFTs/MoS$_2$) yarn electrodes synthesized via hydrothermal approach combined with pre-activation process to carbon fibers represent hierarchical morphology, coaxial structure, high specific area, excellent electrochemical performance, outstanding physical stability and bending flexibility.